Grain Refinement Mechanisms in Gradient Nanostructured AZ31B Mg Alloy Prepared *via* Rotary Swaging

XIN CHEN, CHUMING LIU, YINGCHUN WAN, SHUNONG JIANG, ZHIYONG CHEN, and YONGHAO ZHAO

Gradient nanostructured AZ31B Mg alloy rods were prepared *via* cold rotary swaging in this study. The swaged sample exhibited the best strength-elongation combination published for the AZ31B Mg alloy. Grain refinement mechanisms during deformation were explored using transmission electron microscopy. The results show that in the initial stage high-density deformation twins first divided the coarse grains into a fine lamellar structure; subsequently, massive dislocation arrays further refined the twin lamellae into finer subgrains; finally, randomly oriented nanograins formed *via* dynamic recrystallization caused by both deformation heat and increased stored energy. The gradient microstructure along the radial direction was mainly formed by different loading modes. The grains at the center were subjected to loading almost equally from all radial directions, while those at the edge experienced loading only from one direction.

I. INTRODUCTION

MAGNESIUM alloys possess superior specific stiffness and strength as well as damping capacity.[1] However, their comparably low strength limits their wide industrial applications. In the past few decades, grain refinement has been proven to be one of the most effective methods to improve the strength of Mg alloys mainly *via* various severe plastic deformation (SPD) techniques such as multidirectional forging (MDF),[2] high-ratio differential speed rolling,[3] equal-channel angular pressing,[4] high-pressure torsion (HPT)[5] and surface mechanical attrition treatment (SMAT).[6] HPT and SMAT are the most effective grain refinement methods for achieving nanosized grains.[5,6] However, the sizes of the samples processed by HPT and SMAT are normally ≤ 1 mm in thickness, strongly limiting their application as engineering structural components. In addition, these SPD techniques are complex, expensive and inefficient.[7]

Rotary swaging, as a net-shape forming technology for processing metals and alloys with insufficient cold workability,[8] has been recently reported, showing great potential in substantial grain refinement of metal materials.[9–11] Gan *et al.*[11] showed the remarkable grain refinement of pure Mg after rotary swaging, in which the grain size was refined from 4.5 mm to 25 μm. The working principle of rotary swaging is schematically shown in Figure 1. Two to four dies are usually arranged uniformly around the circumference of the alloy rod. The swaging dies undergo high-speed rotation around the rod and simultaneously perform high-frequency short-range strokes along the radial direction. Figure 1(b) shows the longitudinal cross section with the dies closed during one rotary swaging stroke. Figure 1(b) shows that the swaged rod contains three different zones, including the undeformed zone, the swaging zone and the sizing zone. The main diameter reduction of the swaged rod occurs in the swaging zone.

For most Mg alloys, changing the loading direction has been reported to be an effective way to refine grains.[12–16] Specifically, reverse differential speed rolling, in which the plate is rotated 180 deg along the rolling direction after each rolling pass, has been reported to produce finer grains of AM31 Mg alloy

---

XIN CHEN is with the School of Materials Science and Engineering, Central South University, Changsha 410083, China and also with the Light Alloy Research Institute, Central South University, Changsha, 410083, China. CHUMING LIU, SHUNONG JIANG, and ZHIYONG CHEN are with the School of Materials Science and Engineering, Central South University. YINGCHUN WAN is with the School of Materials Science and Engineering, Central South University; Light Alloy Research Institute, Central South University and also with the School of Metallurgy and Environment, Central South University, Changsha 410083, China. Contact e-mail: ycwanmse@csu.edu.cn YONGHAO ZHAO is with the Nano and Heterogeneous Materials Center, School of Materials Science and Engineering, Nanjing University of Science and Technology, Nanjing 210094, China.
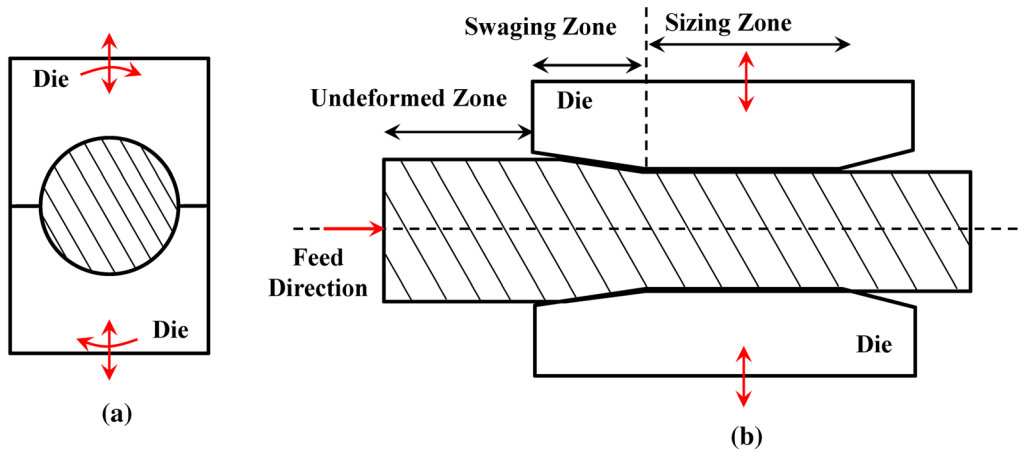
Fig. 1—Working principle of rotary swaging. (*a*) Radial cross section from the top view. (*b*) Longitudinal cross section from the side view, showing three different zones in the rod, including the undeformed, swaging and sizing zones.

than normal differential speed rolling because the change in the strain path results in the formation and intersection of shear bands.[12] Moreover, changing the loading directions in MDF introduces variously oriented and staggered deformation bands, which divide the coarse grains into fine grains in AZ80 Mg alloy.[14] The grain refinement mechanisms of Mg alloys processed by MDF include mechanical twinning, kinking and subsequent dynamic recrystallization (DRX).[15,16] In addition to a change in the loading direction, high strain rate deformation was also reported as another effective method to improve the grain refinement effect of Mg alloys.[17–21] High strain rate deformation could introduce high densities of dislocations and mechanical twins and high stress concentrations near the grain boundaries (GBs) because of the limited recovery time for rate-dependent deformation mechanisms such as cross slipping and GB sliding.[19] For example, more remarkable grain refinement was obtained by high strain rate rolling (9.1 s^{-1}) than by low strain rate rolling (2.9 s^{-1}) in ZK60 alloy because of the higher twin density and the subsequent DRX volume fraction introduced by high strain rate rolling.[20] A similar tendency was also reported in MDF-processed ZK21 alloy under different strain rates (approximately 10^2 and 1 s^{-1}). Enhanced grain refinement was obtained by twin-induced DRX under high strain rate forging.[21]

Recently, we successfully prepared bulk nanocrystalline (NC) Mg–Gd–Y–Zr alloy rods *via* cold rotary swaging with an average grain size of 80 nm and dimensions of $\Phi 3$ mm $\times$ 1000 mm.[22] A detailed microstructural study is still required to shed light on the grain refinement mechanisms during the deformation in rotary swaging. The application of rotary swaging to prepare bulk NC rare-earth-free Mg alloys is worth further exploring.

AZ31B Mg alloy is one of most common commercial rare-earth-free wrought Mg alloys. Precipitation or segregation is limited in AZ31B alloy with increasing temperature because of the low solute concentration. It is an ideal engineering alloy candidate to probe the deformation mechanism influenced by rotary swaging

and the GB-related strengthening mechanism of Mg alloys. In the present work, rotary swaging technology was applied in processing AZ31B Mg alloy at room temperature; consequently, a gradient microstructure with nanograins (NGs) at the center and ultrafine grains (UFGs) at the edge of the swaged rod was obtained. The grain refinement mechanisms during rotary swaging were studied in detail (Table I).

II. MATERIALS AND METHODS

Commercial hot-extruded AZ31B Mg alloy rods with 18 mm diameter and 1000 mm length were employed as the experimental alloys for this work. The microstructure and texture of the as-received alloy rod are shown in Figure 2. The alloy typically exhibits DRX grains with a mean size of approximately 23 μm and a strong basal texture, as shown in Figure 2(b).

The as-received alloy rod was then subjected to multipass cold rotary swaging. In detail, one to five passes of rotary swaging were carried out at room temperature to obtain diameters of 17.80, 17.20 and 16.00 mm for the first, second and final passes, respectively. The deformation degree, ϕ, can be calculated by:

$$\phi = \ln(S_0/S_1) \qquad [1]$$

where S_0 and S_1 are the initial and swaged cross-sectional areas, respectively. ϕ was calculated as 0.02, 0.09 and 0.24 for the first, second and final passes, respectively. The surface temperature of the rods after each swaging pass was measured by an infrared thermometer. To study the microstructural evolution during the swaging process, we interrupted the second swaging pass halfway through.[23] The interrupted swaged sample contained three different zones, including the undeformed, swaging and sizing zones, as schematically presented in Figure 1(b).

Vickers microhardness tests were conducted using an HMV-G 21DT (Shimazdu, Japan) tester with a load of 4.9 N and a dwell time of 15 s. The interval of adjacent measurement points was 0.5 mm. The length of diagonal

indentation ranged from 100 to 120 μm. The microhardness for each point was determined by averaging the values from three indentations. Tensile tests were carried out at room temperature using an Instron 3369 machine with an initial strain rate of 1×10^{-3} s^{-1}. The dog bone-shaped tensile samples were turning machined from the center of the rods, with a gauge length of 15 mm and a gauge diameter of 3 mm or 6 mm. The tensile direction was parallel to the ED. The strain was measured by using a standard noncontact video extensometer. Three tensile specimens were measured to obtain reliable results. The as-received samples were also uniaxially compressed at room temperature to a strain of 0.05 using a Gleeble-1500 machine with a strain rate of 1×10^{-3} or 20 s^{-1}. The compression direction was vertical to the ED.

Transmission electron microscopy (TEM) and high-resolution TEM (HRTEM) observations were carried out on a Tecnai G^2 F20 microscope with an accelerating voltage of 200 kV using a double-tilt specimen stage. All swaged TEM samples were cut vertically to the feed direction, and the uniaxial compression TEM samples were cut along the compression direction. The cut disks were first mechanically ground to a thickness < 100 μm and then thinned by twin-jet polishing to an electron-transparent thickness in an electrolyte containing 1 vol pct nitric acid, 2 vol pct perchloric acid and 97 vol pct ethanol. The twin-jet polishing temperature was approximately − 40 °C. The average grain size was measured by Nano Measurer software, and at least 500 grains were measured for the statistical analysis.

III. RESULTS

A. *Microhardness and Microstructures After Various Swaging Passes*

Figure 3(a) shows the microhardness distribution along the radius of the swaged alloy rods after various swaging passes. First, the as-received alloy has an average microhardness of ~ 46 HV, and the swaged alloys exhibit remarkably increased microhardness. Second, the microhardness gradually increases with increasing swaging passes. Third, the microhardness of the swaged alloys shows a peak distribution with the highest values in the central region and low values in the edge region, and the peak becomes sharper with increasing swaging passes. After the final-pass swaging, the central region exhibits a microhardness as high as 94 HV, which is twice the value of the as-received alloy.

Figures 3(b) through (d) shows the typical microstructure in the central region of swaged alloy rods after the first, second and final swaging passes, respectively. The one-pass swaging process introduces a large number of lamellar deformation twins (which will be identified in Section III–B) with lamellar widths ranging from 100 nm to 1 μm, as shown in Figure 3(b). After two-pass swaging, many nanosized grains or subgrains can be observed, as indicated by the green arrows in Figure 3(c). In addition, some small lamellar twins are still visible, as indicated by the yellow arrows. After the final pass swaging, a completely homogeneous microstructure with equiaxed NGs with an average size of ~ 93 nm is formed. The continuous diffraction rings in the corresponding selected area electron diffraction

Table I. Yield Strength (YS), Ultimate Tensile Strength (UTS) and Elongation to Failure (ε_{ef}) of the Swaged and Initial AZ31B Mg Alloys

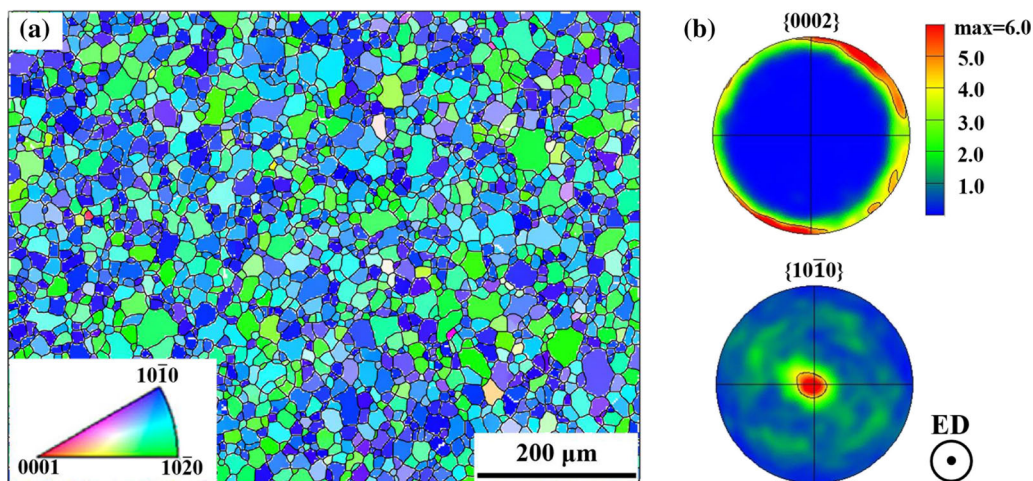| Swaging Pass	YS (MPa)	UTS (MPa)	ε_{ef} (pct)
As Received	203 ± 1	276 ± 1	17.0 ± 0.2
Second Pass	425 ± 31	438 ± 11	8.4 ± 1.7
Final Pass (Φ3 mm)	491 ± 16	539 ± 13	7.1 ± 0.7
Final Pass (Φ6 mm)	463 ± 5	507 ± 4	10.5 ± 0.2

Mechanical data are the average of three measurements.

Fig. 2—Microstructure and texture of the as-received AZ31B alloy rod: (*a*) Inverse pole figure. (*b*) {0002} and {10$\bar{1}$0} pole figures. The extrusion direction (ED) is vertical to the paper.
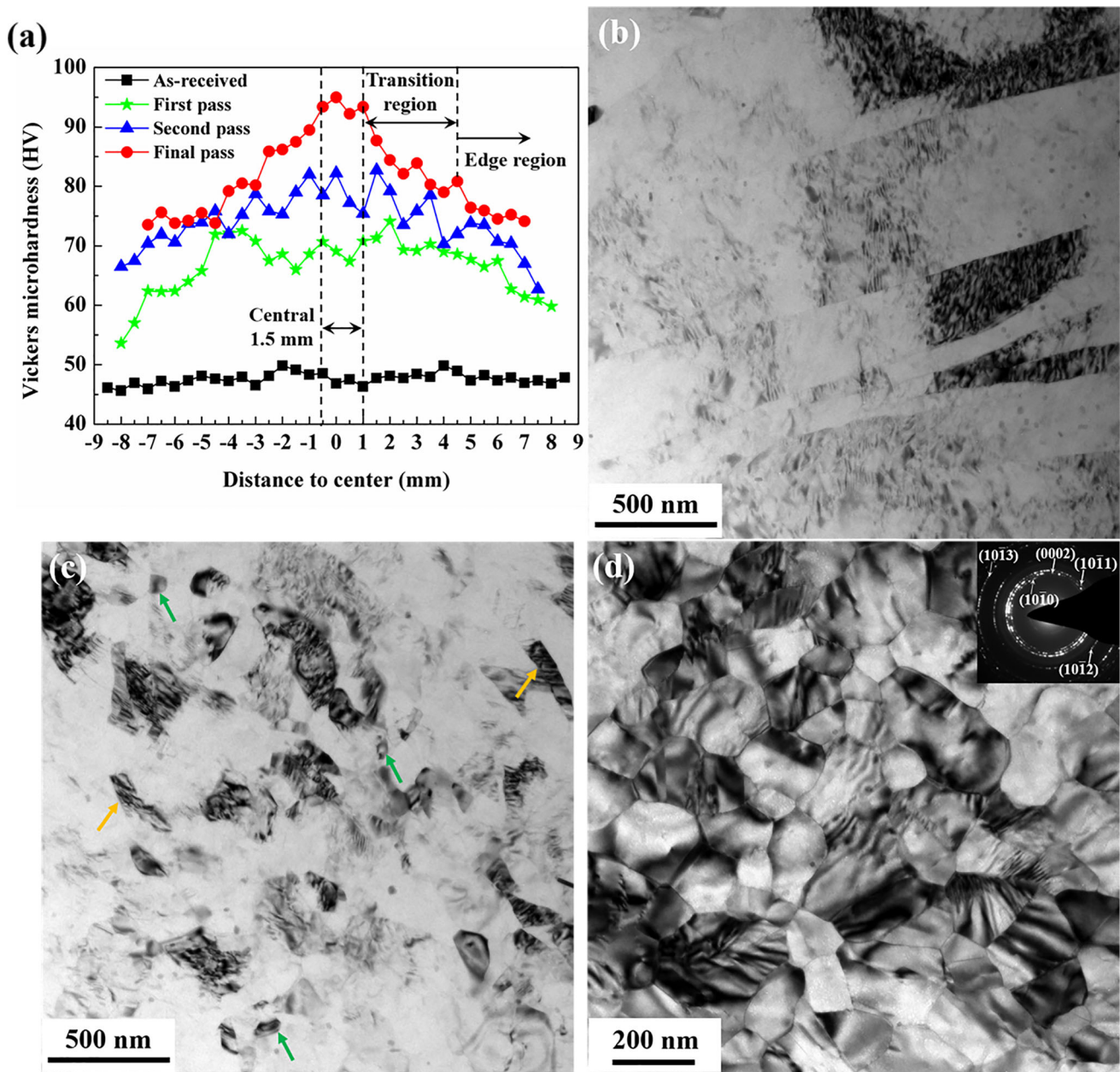
Fig. 3—(*a*) Vickers microhardness distribution of the AZ31B Mg alloy along the radial direction after different swaging passes. (*b*) through (*d*) TEM images observed in the central region of the swaged alloy rods after the (*b*) first, (*c*) second and (*d*) final swaging passes. The selected area electron diffraction (SAED) pattern of the samples after the final swaging pass is also provided as the inset in (d), showing the random orientation of the grains (Color figure online).

(SAED) pattern, as shown by the inset in Figure 3(d), indicate that the NGs are randomly oriented. The sharper and clearer boundaries compared with those in Figure 3(c) also indicate that the subgrain boundaries have evolved to high-angle GBs.

B. *Microhardness and Microstructural Evolution in the Axial Direction During Second Pass Swaging*

According to the above results, NGs first appeared after second pass swaging, suggesting that the second pass is a critical pass for nanocrystallization of AZ31B Mg alloys. Therefore, we intentionally interrupted the

swaging process during the second pass to obtain samples with three different zones, as shown in Figure 1(b). Subsequent microstructural characterizations were performed in these zones to uncover the nanocrystallization mechanism during rotary swaging.

1. *Microhardness Distribution in the Deformation Zone*

Figure 4(a) presents the microhardness distribution in the deformation zone (including swaging and sizing zones) of the interrupted two-pass swaged sample. The microhardness is 65 HV at the starting location of the swaging zone (position A in Figure 4(b)), and it
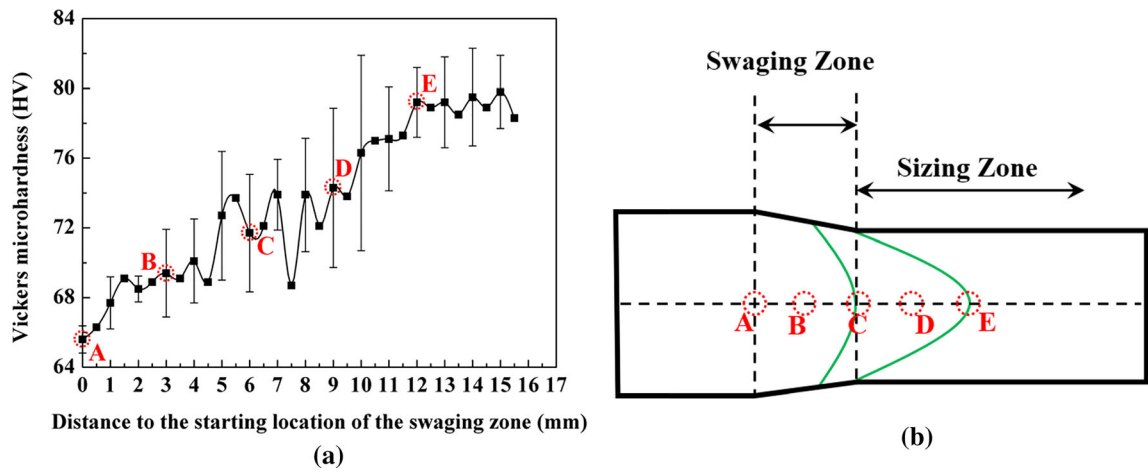
Fig. 4—(*a*) Microhardness distribution in the deformation zone of the interrupted two-pass swaged sample. (*b*) Schematic representation of the corresponding positions from A to E determined in (a). Positions A and C represent the starting locations of the swaging zone and sizing zone, respectively. Position E represents the position at which constant hardness begins. Positions B and D are the midpoints of AC and CE, respectively (Color figure online).
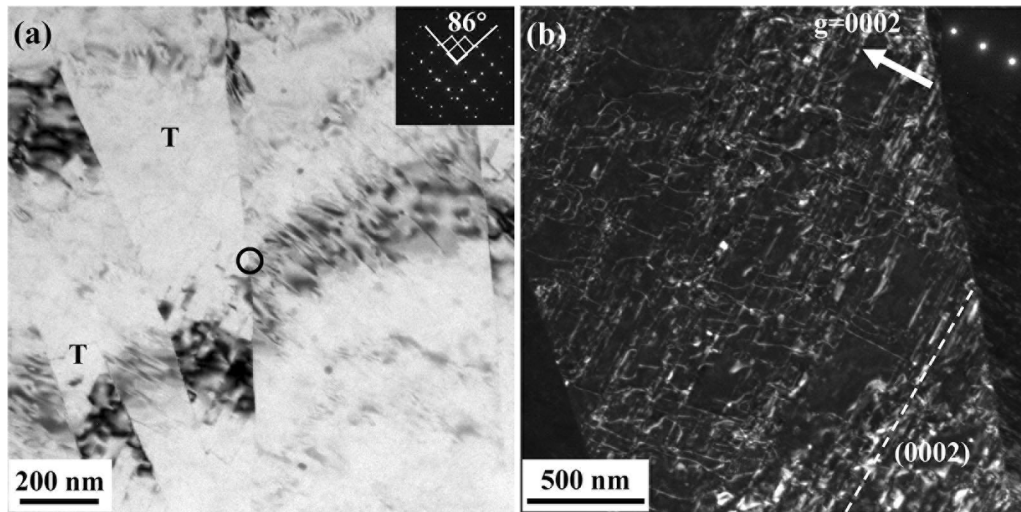

Fig. 5—(*a*) Typical TEM image showing a lamellar deformation twin at position A. The corresponding SAED pattern of the circled area in the inset reveals a {10$\bar{1}$2} tension twin with a misorientation of ~ 86 deg at the TB. (*b*) Dark-field TEM image showing non-basal dislocations in the twin lamella. The two-beam pattern is provided as an inset in (b).

gradually increases when moving the microhardness test position toward the sizing zone and then remains nearly constant at approximately 79 HV after position E. The starting location of the sizing zone is marked as C. Positions B and D correspond to the midpoints of AC and CE, respectively, as schematically shown in Figure 4(b). The highest microhardness (position E) is located in the sizing zone rather than at the end of the swaging zone (position C), which is attributed to the higher velocity of material flow at the center of the rod, as shown by the simple material flow lines (green lines) drawn in Figure 4(b).

2. *Microstructural Evolution in the Deformation Zone*

The microstructural evolution in the above deformation zone from positions A to E was then characterized by TEM. Figure 5(a) presents a typical morphology of

the lamellar twin structure at position A, which is similar to the lamellar structure shown in Figure 3(b). Based on a random SAED analysis of ten twin lamellae, most of the deformation twins are determined to be {10$\bar{1}$2} tension twins (as indicated by "T" in the figure) with a misorientation of ~ 86 deg at the twin boundary (TB). Within the twin lamellae, when viewing from $g = (0002)$ in the dark-field condition, dislocations are observed on the prismatic and pyramidal planes, as shown in Figure 5(b). Based on the g·b criterion, the dislocations visible with $g = (0002)$ have a $\langle c \rangle$ component and are most likely $\langle c + a \rangle$ dislocations, as a pure $\langle c \rangle$ dislocation has extremely low mobility.

At position B, deformation twins are much more frequently observed, as shown in Figure 6(a). The initial coarse grains are divided into fine lamellar structures by dense twin lamellae. A high density of dislocations is
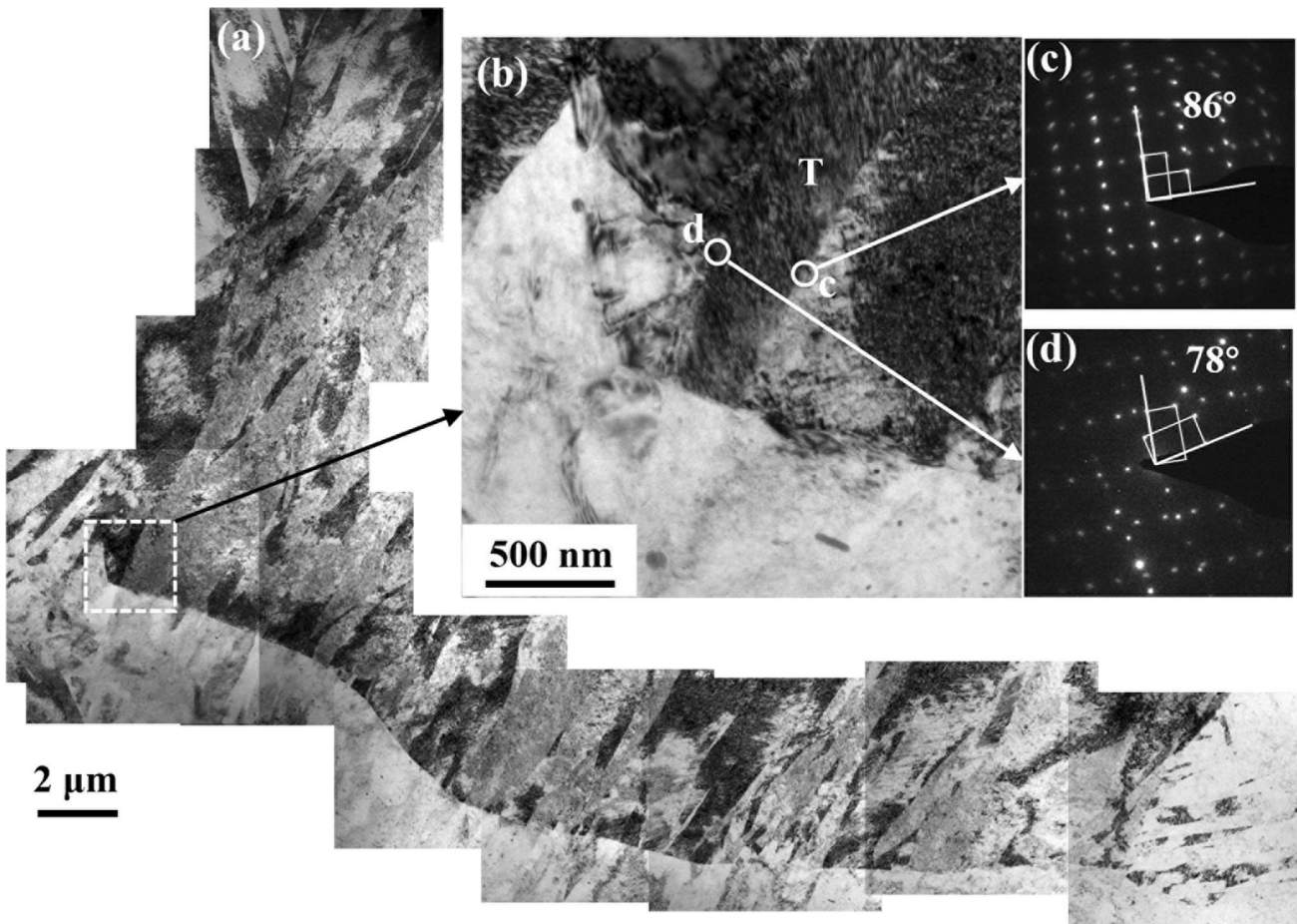
Fig. 6—(*a*) Typical TEM image showing a dense distribution of deformation twins at position B. (*b*) Magnified TEM image of the white dotted box in (a). The corresponding SAED patterns of the TB areas in (b) are shown in (*c*) and (*d*). The SAED patterns reveal misorientations of 86 deg and 78 deg with the matrix in (c) and (d), respectively.

observed in the interior of the twins, as shown in Figure 6(b). The corresponding SAED patterns near the TBs in Figure 6(b) are shown in Figures 6(c) and (d). Boundary c in Figure 6(b) has a nearly ideal misorientation of tension twins. Boundary d has a zigzag appearance and a misorientation of 78 deg with the matrix. In addition, many basal stacking faults (SFs) are found within the twin lamellae, as indicated by the white arrows in Figure 7(a). The HRTEM image of the white dotted box in Figure 7(a) further reveals $\{10\bar{1}2\}$ tension twins with a TB misorientation of 86 deg and basal SFs within the twin lamellae.

At position C, most TBs become curved because of the interaction with dislocations.[24] Several dislocation arrays are also observed within twin lamellae, as indicated by the red arrows in Figure 8(a). The twin lamellae are divided into fine subgrains with dimensions varying in the range of 30 to 300 nm. Moreover, a $\{10\bar{1}1\}$ contraction twin with a misorientation of 56 deg at the TB is also observed, as identified by the SAED pattern in Figure 8(b) and the HRTEM analysis in Figure 8(d). The arc diffraction spots at 5 deg suggest that the contraction twin is also divided into fine units by dislocation arrays. Furthermore, a small fraction of tension twin lamellae with a width < 100 nm is also

observed without any further refinement, as indicated by "T" in Figure 8(a) and identified by the SAED pattern in Figure 8(c), because of the difficulty of dislocation propagation and motion in crystallites with sizes finer than 100 nm.[25]

At position D, many newly formed NGs with sharp and clear boundaries as well as uniform contrast in the grain interiors are observed, as indicated by the green arrows in Figure 9(a). Magnified HRTEM images of the NG in the white dotted box of Figure 9(a) are shown in Figures 9(b) through (d). The NG has a GB misorientation of 21 deg in the (0001) plane with its upper neighboring grain, marked as "B1" in Figure 9(b), as revealed in Figure 9(c), and has a GB misorientation of 28 deg in the (0001) plane with its lower neighboring grain, marked as "B2" in Figure 9(b), as revealed in Figure 9(d). The uniform contrast in the grain interiors of these NGs indicates that they are free of deformation lattice imperfections such as dislocations. Therefore, the features of high-angle GBs and the absence of deformation defects in the NGs imply that they were formed through DRX.

At position E, where the alloy possesses the highest hardness within the deformation zone, more NGs can be formed, as indicated by the green arrows in Figure 10.
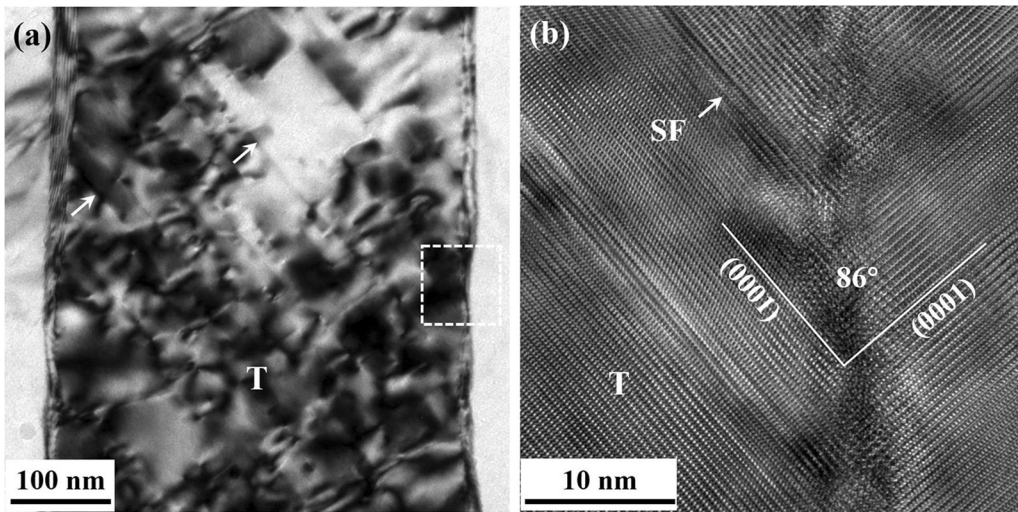
Fig. 7—(a) TEM image of the twin with many SFs (white arrows) observed at position B. (b) HRTEM image of the white dotted box in (a), further showing {10$\bar{1}$2} tension twins with a TB misorientation of 86 deg and basal SFs within the twin lamella.
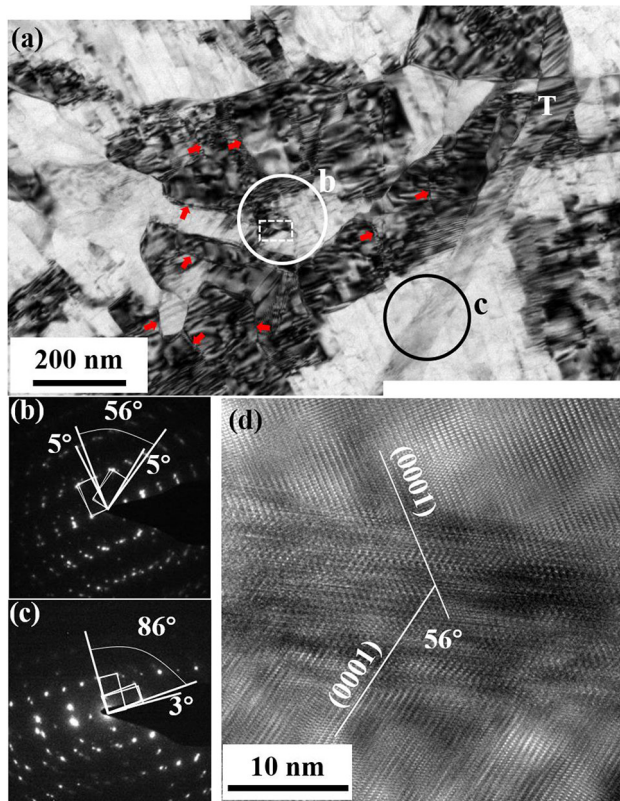

Fig. 8—(a) Typical TEM image at position C showing the refinement of twin lamellae by a high density of dislocation arrays, as indicated by the red arrows. The SAED patterns of the corresponding circles "b" and "c" in (a) are provided in (b) and (c), respectively, revealing the orientation relationships of the {10$\bar{1}$1} contraction twin and {10$\bar{1}$2} tension twin. (d) HRTEM image of the white dotted box in (a) showing a {10$\bar{1}$1} contraction twin with a TB misorientation of 56 deg (Color figure online).

Moreover, some fine twin lamellae are still observed without further refinement. The arcing in the SAED pattern indicates a relatively high difference in misorientation between the NGs and twins.

C. Tensile Properties of the Swaged and Initial AZ31B Mg Alloys

The engineering stress–strain curves for swaged AZ31B Mg alloys under uniaxial tension at room temperature are presented in Figure 11(a). Figure 11(a) shows that in the central region with a diameter of 3 mm, the yield strength significantly increases from 203 MPa to 425 MPa after the two-pass swaging. After the final-pass swaging, the yield strength and the ultimate strength reach 491 MPa and 539 MPa, respectively, and the elongation to failure is reduced to 7.1 pct. For tensile samples with a gauge diameter of 6 mm, the yield and ultimate strength of the swaged AZ31B alloy after the final pass slightly decrease to 463 and 507 MPa, respectively. In contrast, the elongation to failure increases to 10.5 pct. The enhanced elongation to failure can be mainly attributed to the gradient microstructure obtained along the radial direction and the smaller volume fraction of NGs in the sample with a larger gauge diameter.

Figure 11(b) shows a comparison of the high-strength AZ31B Mg alloys fabricated through different SPD technologies.[26–33] The AZ31B alloy prepared via cold rotary swaging has the highest yield strength with good ductility in comparison with those alloys prepared by other SPD technologies.

IV. DISCUSSION

A. Grain Refinement Mechanisms

The above microstructural evolution within the deformation zone of the interrupted two-pass swaged sample (Figures 5, 6, 7, 8, 9, and 10) indicates that both deformation twinning and dislocation slip play dominant roles in the grain refinement of AZ31B Mg alloys. In this section, comprehensive discussions of the deformation and grain refinement mechanisms during rotary swaging will be presented.
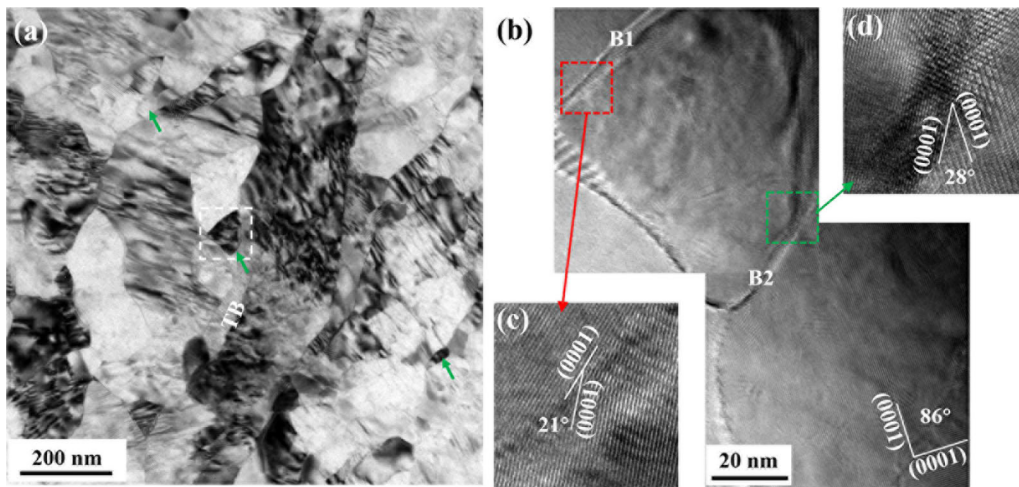
Fig. 9—(a) Typical TEM image at position D showing newly formed DRX NGs with sharp and clear boundaries, as indicated by the green arrows. (b) Magnified HRTEM image of the DRX NG in the white dotted box in (a). (c, d) HRTEM images of the GBs marked as B1 and B2 in (b) revealing 21 and 28 deg crystal misorientations of the DRX NG with its neighboring grains, respectively (Color figure online).
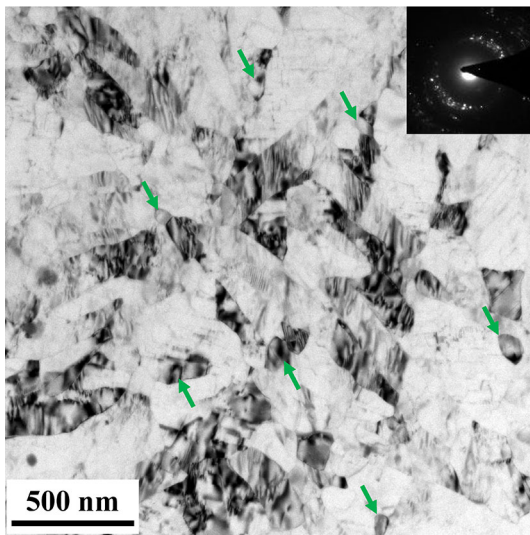

Fig. 10—Typical TEM image showing more NGs formed at position E, as indicated by the green arrows. The SAED pattern provided as an inset reveals a relatively random crystal orientation (Color figure online).

1. Refinement of the Coarse Grains

In the initial stage of rotary swaging, numerous $\{10\bar{1}2\}$ tension twins along with a small fraction of $\{10\bar{1}1\}$ compression twins are formed (Figures 6, 7, 8), which divide the initial coarse grains into dense lamellar structures. In the literature, deformation twinning was considered to contribute to nanocrystallization in Mg–Gd–Y–Zr alloys during the HPT process[34] and in AZ91D alloys during the SMAT process.[6] The high density of deformation twins in the SMATed alloy was considered to originate from the high strain rate (approximately 10^2 to 10^3 s^{-1}).[6] Enhanced twin density has also been observed with increasing applied strain rate in AZ31B Mg alloys.[35] In the present work, the strain rate during rotary swaging is estimated to be 10 to 10^2 s^{-1}, which tends to produce twinning deformation.

To further evaluate the influence of the applied strain rate on the formation of twins, uniaxial compression with strain rates of 10^{-3} and 20 s^{-1} was performed on the as-received AZ31B Mg alloy. After being compressed at a strain rate of 10^{-3} s^{-1}, only a small quantity of twins ≥ 1 μm in width is observed, as shown in Figure 12(a). In contrast, numerous twins are observed after compression at a strain rate of 20 s^{-1}, as shown in Figure 12(b), which are similar in size to those formed after one-pass rotary swaging (Figures 3(b) and 5(a)). This result confirms that the high strain rate is a key factor in the formation of fine and dense twin lamellae.

Generally, $\{10\bar{1}2\}$ tension twins more easily form because of their lower critical resolved shear stress (CRSS) compared to compression twins.[36] Thus, most twin lamellae observed in the initial stage of swaging belong to $\{10\bar{1}2\}$ tension twins, and only a very small number of compression twins are generated. In addition, a 78 deg rotation angle is observed at the interface of the tension twins (Figure 6). This uncommon twin interface has also been observed in ballistic impact Mg–Gd–Y–Zr alloys and was considered a result of accommodation of local strain after twinning.[37,38] Therefore, the poor deformation coordination of Mg alloy and high strain rate during the SPD process resulted in the formation of the uncommon rotated tension twins.[37]

Another important factor in the formation of dense twin lamellae during rotary swaging is the high-frequency change in the loading direction. Activation of twinning is highly dependent on the included angle between the loading direction and the *c*-axis in the grains of Mg alloys. In the literature, the MDF process with three alternative loading directions was confirmed to have a great grain refinement effect on Mg alloys.[39,40] A constant change in the loading direction in the MDF process resulted in a constant change in the shear stress direction and facilitated activation of multiple twins.[39,40] Compared with the MDF process,
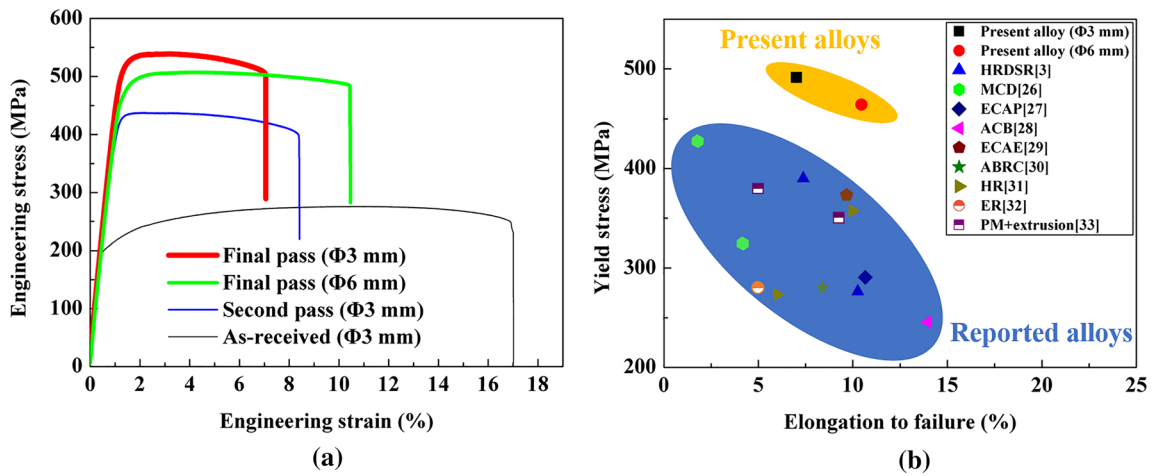
Fig. 11—(a) Room-temperature engineering stress–strain curves of swaged AZ31B Mg alloys under uniaxial tension. The tensile samples after the final pass have a gauge diameter of 3 mm or 6 mm. (b) Comparison of high-strength AZ31B Mg alloys fabricated through various SPD technologies.[3,26–33] HRDSR: high-ratio differential speed rolling, MCD: multipass cold drawing, ECAP/E: equal-channel angular pressing/extrusion, ACB: accumulative compression bonding, ABRC: alternate biaxial reverse corrugation, HR: hot-roller-cold-material rolling, ER: electroplastic rolling, PM: powder metallurgy.
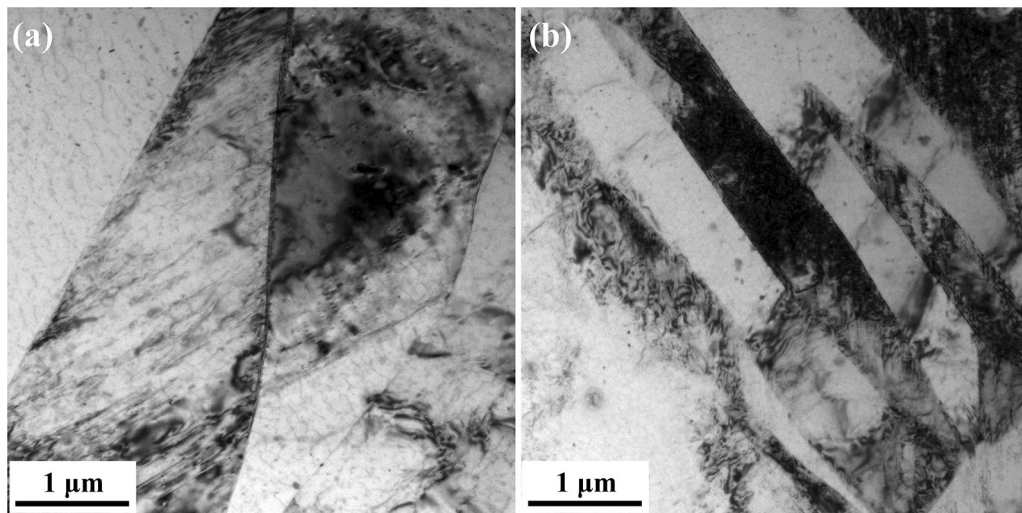

Fig. 12—Typical TEM images showing microstructures of the uniaxial compression samples with a strain of 0.05 and strain rates of (a) 10^{-3} s^{-1} and (b) 20 s^{-1}.

the much higher frequency of change in the loading direction in the rotary swaging dramatically increases the opportunity for the resolved shear stress to exceed the CRSS for twinning in every grain. This results in more multiple twinning. Briefly, both the high strain rate and the high-frequency change in the loading direction led to the formation of dense twin lamellae in the swaged alloy with a relatively low deformation degree of $\phi = 0.09$.

2. Refinement of Twin Lamellae

The microstructure at position C (Figure 8) shows that twin lamellae can be further refined into fine subgrains with dimensions ranging from 30 to 300 nm. Figures 13(a) and (c) further displays that numerous dislocation arrays form the low-angle GBs of the subgrains, as indicated by the red arrows. Similar results

have been reported by Shi et al. in the study of grain refinement during the SMAT process.[6] The small misorientation of ~ 5 deg identified in Figure 13(b) further confirms that these dislocation arrays do not significantly affect the orientations of the fine subgrains. When the strain energy continues to increase to a sufficiently high value, these dislocation arrays lead to the occurrence of DRX.[6]

Dislocation arrays in Mg alloys are considered to stem from the piling up of non-basal dislocations,[6,41,42] which are easily activated at positions where local stress concentrations exist.[43] Indeed, TEM observations and molecular dynamics simulations of polycrystalline Mg indicated that non-basal dislocations, such as prismatic and pyramidal $\langle c + a \rangle$ dislocations, are activated as a result of high compatibility stresses at GBs and TBs.[44,45] Here, in the swaged alloy, after the formation
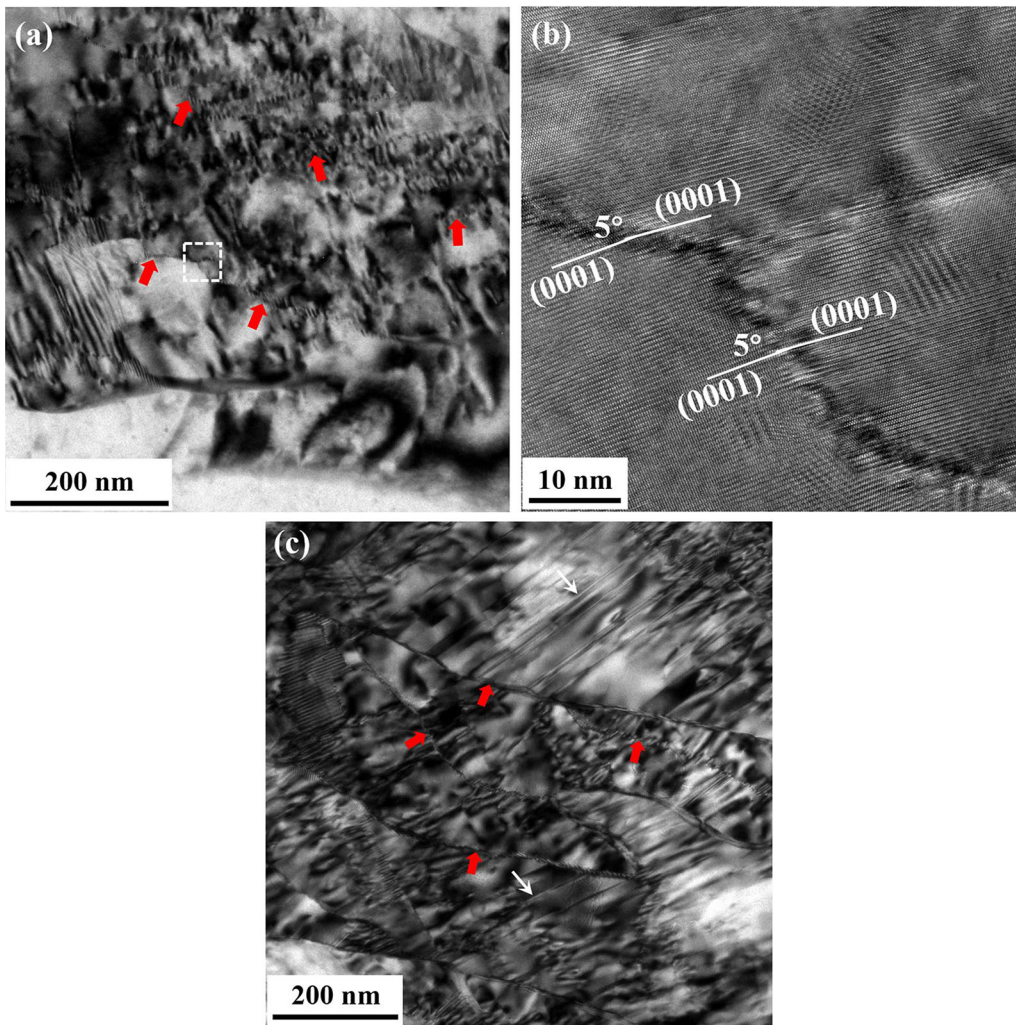
Fig. 13—(a) TEM image at position C of the interrupted two-pass swaged sample showing numerous dislocation arrays within a twin lamella, as indicated by the red arrows. (b) Magnified HRTEM image of the white dotted box in (a) showing a 5 deg small-angle GB formed by dislocation arrays. (c) TEM image at position C further showing many basal SFs (as indicated by the white arrows) around the dislocation arrays.

of numerous twin lamellae, the deformation is localized in the vicinity of the TBs, and the local stress easily becomes high enough to activate non-basal slip.[43,46] In addition, the increase in temperature caused by the heating effect during swaging reduces the CRSS for non-basal slip. Thus, numerous dislocations on prismatic and pyramidal planes are observed (Figure 5(b)). Dislocation arrays are formed as a result of their further multiplication and interaction with basal dislocations.

Figures 7 and 13(c) show many SFs within the deformation twins. Zhang et al. also observed a high density of basal SFs across the whole twin in AZ31B Mg alloy under high strain rate deformation.[47] Most basal SFs observed within twins are formed during twin nucleation and growth in Mg alloys.[24] They can act as heterogeneous nucleation sites for non-basal dislocation,[48,49] contributing to enhanced activity of non-basal

dislocation slip and formation of numerous dislocation arrays within the twin lamellae.

3. Dynamic Recrystallization

After two-pass swaging, clean and strain-free NGs with high-angle GBs are obtained, as shown in Figures 9 and 10. Compared with the serrated boundaries of dislocation arrays, these high-angle GBs of NGs are much sharper. The only possible way to generate such clean crystallites within a heavily deformed area is DRX.[6] The surface temperatures of the swaged rod measured by an infrared detector are approximately 80 °C, 140 °C and 110 °C immediately after the first, second, and final swaging passes, respectively. The central part would logically have a higher temperature than the surface due to its noncontact with the environment. Additionally, the ultrahigh strain and stored

energy generated by severe dislocation multiplication and accumulation in the central region would significantly decrease the DRX temperature. When the temperature at the center is higher than the DRX temperature, DRX occurs, and NGs are formed.

4. *Nanocrystallization Mechanisms of AZ31B Mg Alloy During Rotary Swaging*

Based on the above discussion, the grain refinement process in AZ31B Mg alloy during rotary swaging can be concluded to consist of three important steps. (1) The high density of twin lamellae, mostly tension twins and a small quantity of compression twins, introduced by the high strain rate and the high-frequency change in loading direction, segments the initial coarse grains into a fine lamellar structure. (2) Numerous dislocation arrays, resulting from the piling up of basal and non-basal dislocation, further divide the twin lamellae into ultrafine subgrains. (3) The occurrence of DRX,

due to the deformation heat and increased strain and stored energy, promotes the formation of randomly oriented NGs.

B. *Gradient Microstructure Along the Radial Direction*

As shown in Figure 3, the swaged samples have a gradient distribution of microhardness along the radial direction. The microhardness gradually increases from the edge to the center. To uncover the underlying reasons, TEM observation was performed to further characterize the microstructures of the final-pass swaged sample in different regions along the radial direction, as shown in Figure 14. The transition region with a 2 mm distance to the center exhibits an obvious gradient microstructure with NGs in the bottom half of Figure 14(a) (indicated by "NG") and UFGs (100 nm to 1 μm) in the top half of Figure 14(a) (indicated by "UFG"). The transition region with a 4 mm distance to
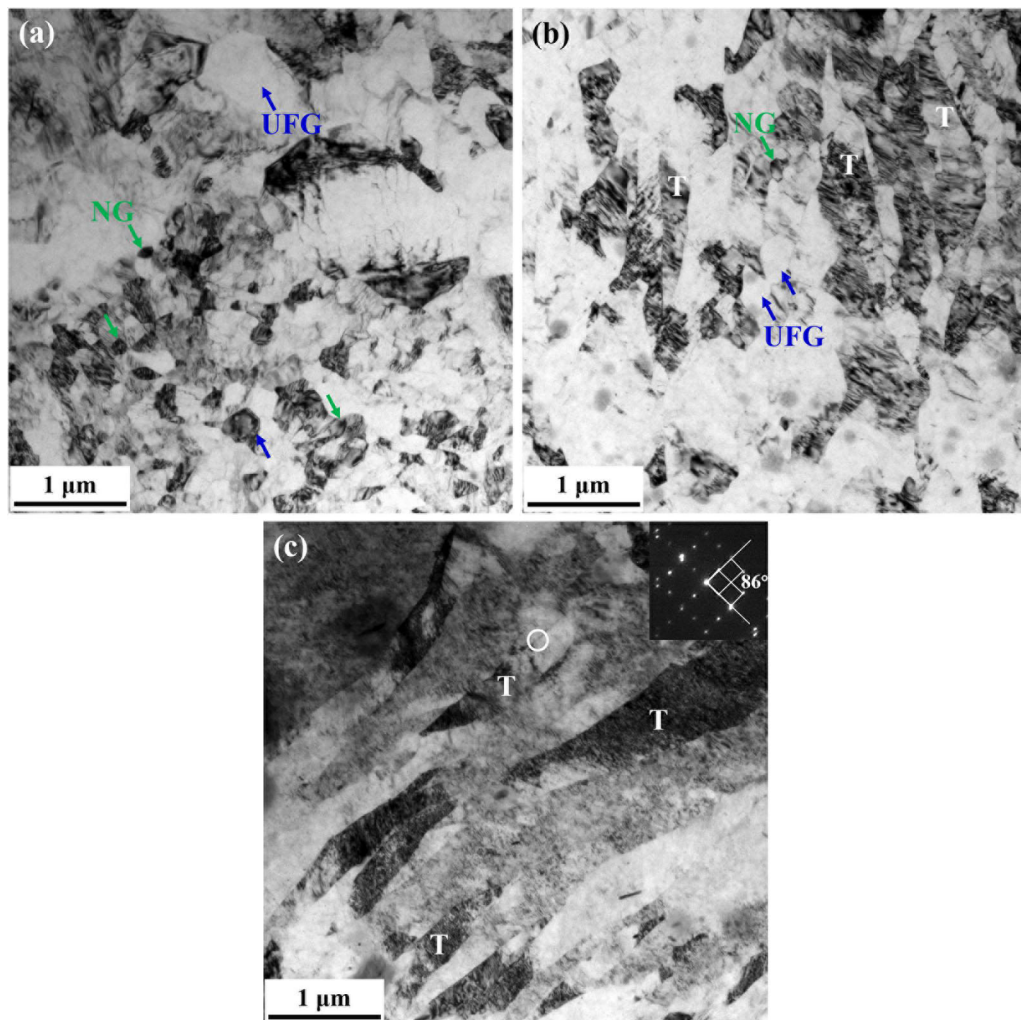

Fig. 14—TEM images at different radial positions of the swaged alloy rod after the final swaging pass. (*a*) Microstructure in the transition region with a distance to the center of approximately 2 mm, showing a gradient microstructure with NGs and UFGs. (*b*) Microstructure in the transition region with a distance to the center of approximately 4 mm, showing another gradient microstructure with NGs, UFGs and deformation twins. (*c*) Microstructure in the edge region with a distance to the center of approximately 6.5 mm, showing only the existence of twin lamellae. The SAED pattern in the inset of (*c*) reveals that these twins formed in the edge region are also {10$\bar{1}$2} tension twins.
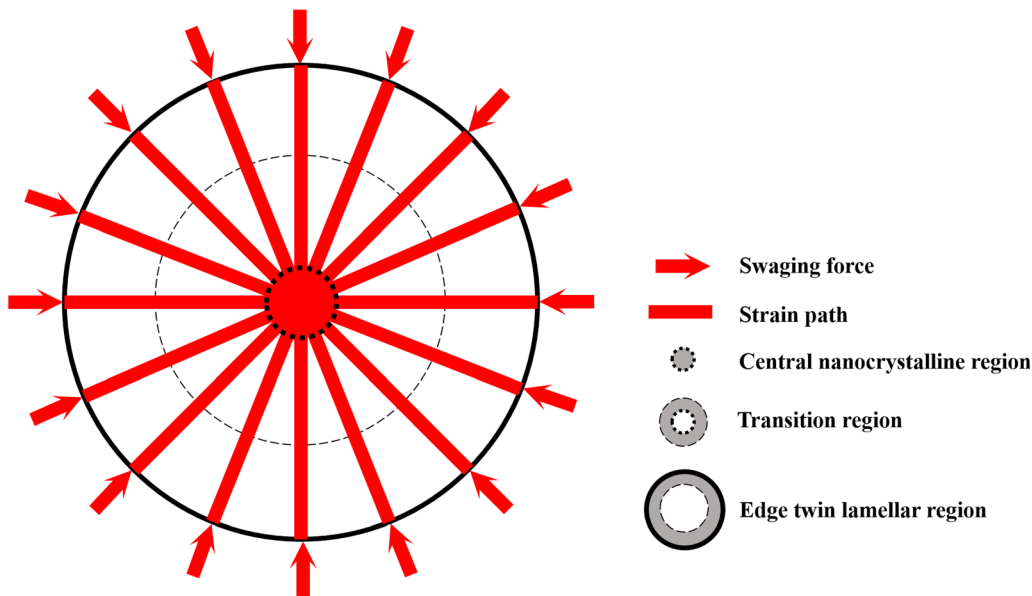
Fig. 15—Schematic representation of the loading mode during rotary swaging.

the center exhibits another gradient microstructure containing mostly twin lamellae (indicated by "T") and UFGs as well as a small quantity of NGs. The edge region with a 6.5 mm distance to the center consists of many twin lamellae, similar to those shown in Figure 6(a). Hence, the increased microhardness from the edge to the center is the result of the gradually increased grain refinement process along the radius. Similar grain refinement along the radius has also been observed in rotary swaged RR1000 nickel alloys[10] and pure Mg,[11] where no explanation or speculation was proposed.

Here, we consider that the above gradient features of microstructure and microhardness can be ascribed to the unique loading mode during rotary swaging. Figure 15 illustrates the loading mode within the swaging zone. The loading mode for each impact is similar to that in uniaxial compression. If we equally divide the rod into different fan-shaped parts, then every part experiences uniaxial compression during each impact. The compressive loading time mainly depends on the frequency of one stroke. For a certain part, the grains at the edge region tend to deform under unidirectional loading along the radial direction, resulting in a single specific shear direction, even if hundreds or thousands of strokes are applied after the final-pass swaging. Thus, only twins can be formed in the edge region (Figure 14(c)). In contrast, for the central region, the loading mode periodically changes with multiple directions along the radial direction, containing almost all radial directions, which leads to more shear directions and strain gradients within the grains.[50] This induces further refinement of the twin lamellae by dislocation arrays. Through DRX, the subgrains surrounded by dislocation arrays finally transform into NGs with high-angle GBs. Logically, the fewer loading directions in the transition region would result in a weaker refinement than that in the central region, as confirmed by Figures 14(a) and (b).

V. CONCLUSIONS

In summary, high-strength AZ31B Mg alloy rods with nanograins at the center and ultrafine grains in the transition region were prepared *via* rotary swaging at room temperature. The grain refinement mechanism during rotary swaging was studied based on the microstructure evolution within the deformation zone as well as the gradient microstructure along the radius of the swaged alloy rod. The following conclusions can be made:

1. Rotary swaging significantly enhanced the microhardness of AZ31B alloy and resulted in a peak distribution with the highest value at the center and the lowest value at the edge. The hardness peak became sharper with increasing swaging pass. After the final swaging pass, the sample with a gauge diameter of 6 mm showed a yield strength, ultimate strength and elongation to failure of 463 MPa, 507 MPa and 10.3 pct, respectively.

2. The second swaging pass played a key role in grain refinement. The nanocrystallization process of AZ31B Mg alloy during rotary swaging can be divided into three steps. First, dense twins refined the initial coarse grains into a fine lamellar structure. Then, numerous dislocation arrays further divided the twin lamellae into finer subgrains. Finally, dynamic recrystallization occurred, forming randomly oriented nano-grains.

3. A gradient microstructure was generated along the radius after rotary swaging. In the central region with a diameter of approximately 1.5 mm, nanograins with an average grain size of approximately 93 nm were formed. In the transition region, a mixed microstructure containing nanograins, ultrafine grains and twin lamellae was obtained. In the edge region, only dense twin lamellae were observed. The different refinement effects along

the radius are attributed to their different loading modes during rotary swaging.

CONFLICT OF INTEREST

On behalf of all authors, the corresponding author states that there is no conflict of interest.

REFERENCES

1. T.M. Pollock: *Science*, 2010, vol. 328, pp. 986–87.
2. B.B. Dong, X. Che, Z.M. Zhang, J.M. Yu, and M. Meng: *J. Alloys Compd.*, 2021, vol. 853, pp. 157066, 1–12.
3. W.J. Kim, Y.G. Lee, M.J. Lee, J.Y. Wang, and Y.B. Park: *Scr. Mater.*, 2011, vol. 65, pp. 1105–08.
4. B.Q. Xu, J.P. Sun, Z.Q. Yang, L.R. Xiao, H. Zhou, J. Han, H. Liu, Y. Wu, Y.C. Yuan, X.R. Zhuo, D. Song, J.H. Jiang, and A.B. Ma: *Mater. Sci. Eng. A*, 2020, vol. 780, pp. 139191, 1–11.
5. L.R.C. Malheiros, R.B. Figueiredo, and T.G. Langdon: *J. Mater. Res. Technol.*, 2015, vol. 4, pp. 14–17.
6. H.Q. Sun, Y.N. Shi, M.X. Zhang, and K. Lu: *Acta Mater.*, 2007, vol. 55, pp. 975–82.
7. Y. Estrin and A. Vinogradov: *Acta Mater.*, 2013, vol. 61, pp. 782–817.
8. L. Kunčická, R. Kocich, C. Hervoches, and A. Macháčková: *Mater. Sci. Eng. A*, 2017, vol. 704, pp. 25–31.
9. H. Alkhazraji, E. El-Danaf, M. Wollmann, and L. Wagner: *Adv. Mater. Sci. Eng.*, 2015, vol. 2015, pp. 1–12.
10. M.R. Bache, J. O'Hanlon, P.J. Withers, D.J. Child, and M.C. Hardy: *Metals*, 2016, vol. 6, pp. 54–60.
11. W.M. Gan, Y.D. Huang, R. Wang, G.F. Wang, A. Srinivasan, H.-G. Brokmeier, N. Schell, K.U. Kainer, and N. Hort: *Mater. Des.*, 2014, vol. 63, pp. 83–88.
12. L.L. Chang, S.B. Kang, and J.H. Cho: *Mater. Des.*, 2013, vol. 44, pp. 144–48.
13. L.C. Tang, C.M. Liu, Z.Y. Chen, D.W. Ji, and H.C. Xiao: *Mater. Des.*, 2013, vol. 50, pp. 587–96.
14. J.L. Zhang, H. Xie, Z.L. Lu, Y. Ma, S.P. Tao, and K. Zhao: *Results Phys.*, 2018, vol. 10, pp. 967–72.
15. H. Miura, G. Yu, and X. Yang: *Mater. Sci. Eng. A*, 2011, vol. 528, pp. 6981–92.
16. F.R. Cao, J. Zhang, X. Ding, G.Q. Xue, S.Y. Liu, C.F. Sun, R.K. Su, and X.M. Teng: *Mater. Sci. Eng. A*, 2019, vol. 760, pp. 377–93.
17. H.Q. Sun, Y.N. Shi, and M.-X. Zhang: *Wear*, 2009, vol. 266, pp. 666–70.
18. S.Q. Zhu, H.G. Yan, J.H. Chen, Y.Z. Wu, B. Su, Y.G. Du, and X.Z. Liao: *Scr. Mater.*, 2012, vol. 67, pp. 404–07.
19. I. Ulacia, N.V. Dudamell, F. Gálvez, S. Yi, M.T. Perez-Prado, and I. Hurtado: *Acta Mater.*, 2010, vol. 58, pp. 2988–98.
20. S.Q. Zhu, H.G. Yan, J.H. Chen, Y.Z. Wu, J.Z. Liu, and J. Tian: *Scr. Mater.*, 2010, vol. 63, pp. 985–88.
21. Y.Z. Wu, H.G. Yan, J.H. Chen, Y.G. Du, S.Q. Zhu, and B. Su: *Mater. Sci. Eng. A*, 2012, vol. 556, pp. 164–69.
22. Y.C. Wan, B. Tang, Y.H. Gao, L.L. Tang, G. Sha, B. Zhang, N.N. Liang, C.M. Liu, S.N. Jiang, Z.Y. Chen, X.Y. Guo, and Y.H. Zhao: *Acta Mater.*, 2020, vol. 200, pp. 274–86.
23. M.G. Jiang, C. Xu, H. Yan, G.H. Fan, T. Nakata, C.S. Lao, R.S. Chen, S. Kamado, E.H. Han, and B.H. Lu: *Acta Mater.*, 2018, vol. 157, pp. 53–71.
24. F.L. Wang, C.D. Barrett, R.J. McCabe, H.E.I. Kadiri, L. Capolungo, and S.R. Agnew: *Acta Mater.*, 2019, vol. 165, pp. 471–85.
25. S. Cheng, J.A. Spencer, and W.W. Milligan: *Acta Mater.*, 2003, vol. 51, pp. 4505–518.
26. W.Z. Chen, W.C. Zhang, H.Y. Chao, L.X. Zhang, and E.D. Wang: *Mater. Sci. Eng. A*, 2015, vol. 623, pp. 92–96.
27. W.T. Lee, S.X. Ding, D.K. Sun, C.I. Hsiao, C.P. Chang, L. Chang, and P.W. Kao: *Metall. Mater. Trans. A*, 2011, vol. 42A, pp. 2909–916.
28. J.J. Ma, X.Y. Yang, Q.H. Huo, H. Sun, J. Qin, and J. Wang: *Mater. Des.*, 2013, vol. 47, pp. 505–09.
29. S.X. Ding, W.T. Lee, C.P. Chang, L.W. Chang, and P.W. Kao: *Scr. Mater.*, 2008, vol. 59, pp. 1006–09.
30. Q. Yang and A.K. Ghosh: *Acta Mater.*, 2006, vol. 54, pp. 5159–70.
31. D. Liu, M.Z. Bian, S.M. Zhu, W.Z. Chen, Z.Y. Liu, E.D. Wang, and J.F. Nie: *Mater. Sci. Eng. A*, 2017, vol. 706, pp. 304–310.
32. X.P. Li, X.H. Li, Y.D. Ye, R.K. Zhang, S.-Z. Kure-Chu, and G.Y. Tang: *Mater. Sci. Eng. A*, 2019, vol. 742, pp. 722–33.
33. W.B. Fang, W. Fang, and H.F. Sun: *Powder Technol.*, 2011, vol. 212, pp. 161–65.
34. R. Alizadeh, R. Mahmudi, A.H.W. Ngan, Y. Huang, and T.G. Langdon: *Mater. Sci. Eng. A*, 2016, vol. 651, pp. 786–94.
35. L. Li, O. Muránsky, E.A. Flores-Johnson, S. Kabra, L.M. Shen, and G. Proust: *Mater. Sci. Eng. A*, 2017, vol. 684, pp. 37–46.
36. Y.M. Zhu, S.W. Xu, and J.F. Nie: *Acta Mater.*, 2018, vol. 143, pp. 1–12.
37. X.Y. Shi, A.A. Luo, S.C. Sutton, L. Zeng, S.Y. Wang, X.Q. Zeng, D.J. Li, and W.J. Ding: *J. Alloys Compd.*, 2015, vol. 650, pp. 622–32.
38. L.H. Mao, C.M. Liu, T. Chen, Y.H. Gao, S.N. Jiang, and R.K. Wang: *Scr. Mater.*, 2018, vol. 150, pp. 87–91.
39. M.G. Jiang, H. Yan, and R.S. Chen: *J. Alloys Compd.*, 2015, vol. 650, pp. 399–409.
40. H. Miura, M. Kobayashi, T. Aoba, H. Aoyama, and T. Benjanarasuth: *Mater. Sci. Eng. A*, 2018, vol. 731, pp. 603–08.
41. B.Z. Wang, B. Tang, C. You, Y.C. Wan, Y.H. Gao, Z.Y. Chen, L.W. Lu, C.M. Liu, and J. Wang: *Mater. Sci. Eng. A*, 2020, vol. 775, pp. 138789, 1–11.
42. B. Li, E. Ma, and K.T. Ramesh: *Metall. Mater. Trans. A*, 2008, vol. 39A, pp. 2607–614.
43. B. Li, Q.W. Zhang, and S.N. Mathaudhu: *Scr. Mater.*, 2017, vol. 134, pp. 37–41.
44. D.-H. Kim, F. Ebrahimi, M.V. Manuel, J.S. Tulenko, and S.R. Phillpot: *Mater. Sci. Eng. A*, 2011, vol. 528, pp. 5411–20.
45. S.W. Lee, S.-H. Kim, W.-K. Jo, W.-H. Hong, W. Kim, B.G. Moon, and S.H. Park: *J. Alloys Compd.*, 2019, vol. 791, pp. 700–710.
46. S.Q. Zhu and S.P. Ringer: *Acta Mater.*, 2018, vol. 144, pp. 365–75.
47. X.Y. Zhang, B. Li, and Q. Liu: *Acta Mater.*, 2015, vol. 90, pp. 140–50.
48. K. Wei, L.R. Xiao, B. Gao, L. Li, Y. Liu, Z.G. Ding, W. Liu, H. Zhou, and Y.H. Zhao: *J. Magnes. Alloy*, 2020, vol. 8, pp. 1221–27.
49. S. Sandlöbes, Z. Pei, M. Friák, L.F. Zhu, F. Wang, S. Zaefferer, D. Raabe, and J. Neugebauer: *Acta Mater.*, 2014, vol. 70, pp. 92–104.
50. T. Sakai, H. Miura, A. Goloborodko, and O. Sitdikov: *Acta Mater.*, 2009, vol. 57, pp. 153–62.